

Design of a Low-Phase-Noise 70-/105-GHz Dual-Band VCO With Common Mode Resonance Expansion

Dongxin Ni[✉], Graduate Student Member, IEEE, Zhe Zhao, Graduate Student Member, IEEE,
 Liang Zhou[✉], Senior Member, IEEE, Jian Pang[✉], Member, IEEE,
 and Jun-Fa Mao[✉], Fellow, IEEE

Abstract—This article presents the design of a CMOS-based voltage-controlled oscillator (VCO) operating in both V- and W-bands by fully utilizing the harmonics in Class-F₂₃ tank. An auxiliary common mode (CM) resonance is introduced to Class-F₂₃ structure via a transformer for CM resonance expansion. This transformer serves dual functions, also generating the second harmonic output, thereby enhancing the area efficiency. The proposed CM resonance expansion suppresses the flicker noise upconversion in a wideband without manual harmonic tuning. A Class-F₂₃ VCO without CM expansion is designed and fabricated for comparison. Besides, the challenges in high-frequency harmonic extraction are highlighted and addressed. The proposed VCO is fabricated using 40-nm CMOS technology. The frequency can cover from 69.92 to 73.84 GHz and from 104.88 to 110.75 GHz with tuning ranges of 5.7%. The measured V- and W-band phase noises (PNs) are -102.5 and -92.35 dBc/Hz at 1-MHz offset with figures of merit of -182.5 and -176 dBc/Hz, respectively. The power consumption is 44 mW in an area of 0.36 mm².

Index Terms—Class-F₂₃, common mode (CM), dual band, low phase noise (PN), V-band, voltage-controlled oscillator (VCO), W-band.

I. INTRODUCTION

DEVELOPMENT of high-performance millimeter-wave voltage-controlled oscillators (VCOs) is important for future radar and communication systems. Short-range, high-speed communication systems operate within the V-band, while long-range radar systems typically utilize the W-band.

Manuscript received 22 October 2023; revised 4 January 2024; accepted 5 February 2024. Date of publication 19 February 2024; date of current version 5 September 2024. This work was supported in part by the National Key Research and Development Project under Grant 2023YFB4403802 and in part by the National Natural Science Foundation of China under Grant 62325110 and Grant 62188102. (*Corresponding author:* Liang Zhou.)

Dongxin Ni, Zhe Zhao, Liang Zhou, and Jian Pang are with the State Key Laboratory of Radio Frequency Heterogeneous Integration, Shanghai Jiao Tong University, Shanghai 200240, China (e-mail: winterwisp@sjtu.edu.cn; zzhao6@sjtu.edu.cn; liangzhou@sjtu.edu.cn; pangjian@sjtu.edu.cn).

Jun-Fa Mao is with the State Key Laboratory of Radio Frequency Heterogeneous Integration, Shanghai Jiao Tong University, Shanghai 200240, China, and also with the State Key Laboratory of Radio Frequency Heterogeneous Integration, Shenzhen University, Shenzhen, Guangdong 518061, China (e-mail: jfmao@sjtu.edu.cn).

Color versions of one or more figures in this article are available at <https://doi.org/10.1109/TMTT.2024.3363893>.

Digital Object Identifier 10.1109/TMTT.2024.3363893

Recently, multiband VCOs have demonstrated considerable potential for future multifunctional transceiver systems, effectively harnessing spectrum resources. For example, a 28-/39-GHz dual-band transceiver has been proposed [1], which required a VCO operating at both 28 and 39 GHz. In comparison to design an ultra-wideband VCO, our proposed dual-band VCO exhibits better power consumption, phase noise (PN) performance, and area efficiency.

The most common way to design a dual-band VCO is to switch different oscillation cores [2], [3], [4], [5], [6], [7], [8], [9], [10]. This method demands two pairs of transistors and inductors, along with a switch to toggle between high- and low-frequency bands. However, when it comes to high-frequency dual-band VCO design, this method poses challenges. First, the switch significantly deteriorates the quality (*Q*) factor of resonators and PN. Second, multiple oscillation cores consume a large area, and the coupling effect between multiple resonators is not negligible. In addition, the PN analysis of dual-band VCOs often focuses on the *Q* factor improvement and lacks numerical analysis of flicker noise.

To address these challenges, the harmonic-rich transformer is proposed for high-frequency dual-band VCO design, as it can be designed at low-frequency bands to maintain a relatively high *Q* factor and generate multiresonant peaks, amplifying the desired harmonics without switch. Harmonic-rich single-core VCOs also demonstrate better PN performance and lower $1/f^3$ corner [11].

The Class-F₂₃ transformer stands out as a typical example of a harmonics-rich transformer [12]. It can be tuned to resonate at both the fundamental frequency (f_0) and the third harmonic frequency ($3f_0$). Its inherent common mode (CM) resonance can be aligned with the second harmonic frequency ($2f_0$) to suppress the upconversion of flicker noise [13], [14], [15], [16]. However, aligning f_0 , $2f_0$, and $3f_0$ to three resonant peaks within the Class-F₂₃ transformer introduces great difficulty in measurement, requiring a complex tuning process of the varactors, which may not be practical.

In light of these considerations, we propose a novel design approach by fully utilizing the f_0 – $3f_0$ signals within the Class-F₂₃ tank to achieve a high-frequency dual-band VCO with low PN in a more compact way. First, the f_0 signal is transferred through a transformer to the doubler to form a $2f_0$ output.

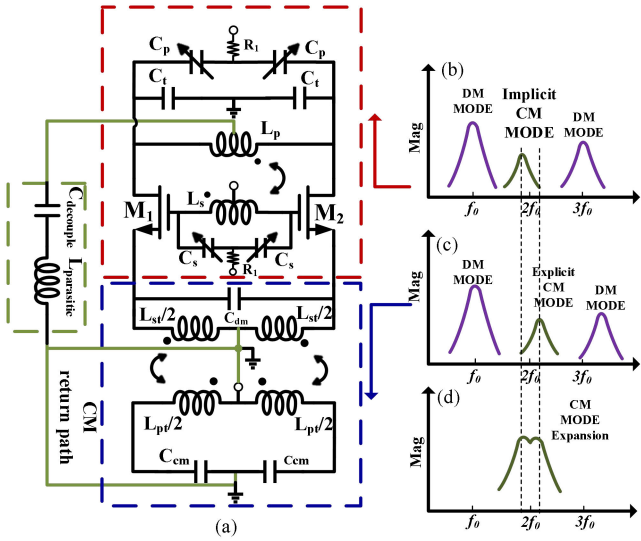


Fig. 1. (a) Schematic of the proposed CM expansion. (b) Magnitude of Z_{11} of the Class-F₂₃ transformer. (c) Magnitude of Z_{11} of the CM expansion transformer. (d) Magnitude of Z_{11} of the expanded CM resonance.

Subsequently, the transformer is reused under CM excitation to introduce an additional CM resonance to the Class-F₂₃ tank, creating CM expansion. This CM expansion effectively suppresses flicker noise upconversion across a broad bandwidth, improving the PN performance in the proposed VCO. Finally, the $3f_0$ signal is amplified by a buffer for direct output.

In comparison to other CM expansion techniques, our approach proves more practical in high-frequency applications. While a transformer designed with multiple couplings is employed to generate CM expansion in the *X*-band [17], its implementation in *V*- or *W*-bands faces challenges due to the reduced size of the transformer and the strict design rule check requirements of CMOS technology. Furthermore, the dual-band frequency in our design exhibits a ratio of 1.5, representing adjacent frequency bands within the millimeter-wave spectrum that are not explored in prior research. Our work extends the available frequency options for mm-wave transceivers.

II. PROPOSED CM EXPANSION

A. Limitations on Class-F₂₃ VCO

A conventional Class-F₂₃ tank is shown in the red dotted box of Fig. 1(a). The transformer demonstrates an implicit CM resonance at $2f_0$ and a differential mode resonance at both f_0 and $3f_0$, as shown in Fig. 1(b).

These resonant frequencies are determined by two ratios, denoted as $X_1 (= (C_p + C_t)/C_s)$ and $X_2 (= C_t/C_p)$ [12]. However, to meet the two specified ratios for X_1 and X_2 , C_t , C_p , and C_s all must be adjustable. This introduces significant challenges in harmonic tuning and constrains the tuning range.

B. Proposed CM Expansion Technique

To obviate the necessity for manual harmonic tuning, a CM expansion transformer [highlighted within the blue dotted box

in Fig. 1(a)] is designed at the source node of the VCO transistor pair. The transformer introduces an explicit CM resonance to the VCO transistor pair, as shown in Fig. 1(c). When the CM return path is well designed with large decoupling capacitor and low-loss metal layers, the power supply can be efficiently shortened to the CM return path for ac signals. This ensures minimal loss within the CM return path, as indicated by the green dotted box in Fig. 1(a).

When we view the circuit from the drain of the VCO transistors to the source, it becomes evident that the CM resonance in the Class-F₂₃ tank and the CM expansion transformer are interconnected in series. Consequently, the overall CM resonance can be regarded as the sum of these two resonances, as depicted in Fig. 1(d), resulting in an expanded bandwidth for the CM resonance.

C. Implementation of Wideband CM Expansion

It is essential to consider the resonant frequencies and *Q* values of the two resonant tanks. Since the resonant frequencies determine the bandwidth and *Q* values determine the flatness within the working band, in this work, two resonant frequencies, 62 and 71 GHz, are selected.

The CM resonant frequency of the Class-F₂₃ tank is chiefly governed by an *LC* network comprising primary windings and capacitors [L_p and C_t in Fig. 1(a)]. This is because the coupling factor between the primary and secondary windings in the Class-F₂₃ transformer under CM excitation is exceedingly small and negligible. Given that the resonant frequency remains fixed within the proposed CM expansion, a high-resistance component, denoted as R_1 , is introduced to mitigate the influence of the varactors [C_p in Fig. 1(a)].

In Fig. 2(a), the layout of the primary winding (L_p) with its associated capacitor is depicted. L_p is designed using top metal layers, while the ground is established through bottom metal layers. For a 50-μm transmission line, its parasitic capacitance measures 28 fF and should not be disregarded. To precisely adjust the implicit CM resonance frequency (71 GHz), two additional capacitors, denoted as C_t , are employed to do the fine-tuning. Finally, with L_p at 80 pH and C_t at 3 fF, the *LC* resonant frequency is calculated to be 71 GHz.

Fig. 2(b) exhibits the layout of the CM expansion transformer. The green arrow represents the CM return path. Here, L_{pt} and L_{st} denote the self-inductances of the primary and secondary transformers, respectively. K_p and K_s represent the self-coupling factors of L_{pt} and L_{st} , respectively, while K_t signifies the coupling factor between the primary and secondary coils. Notably, the current directions on both sides of the capacitor (C_{dm}) are identical, resulting in the cancellation of C_{dm} during CM resonance. The equivalent circuit of CM expansion is depicted in Fig. 2(c), and the parasitic resistance of transformer coils is neglected for simplicity. L_{t1} and L_{t2} represent the CM inductances of $L_{pt}/2$ and $L_{st}/2$, respectively, and their derivation is as follows:

$$\begin{cases} L_{t1} = (1 - K_p)L_{pt}/2 - M_{1-cm} \\ L_{t2} = (1 - K_s)L_{st}/2 - M_{1-cm} \\ M_{1-cm} = K_t \sqrt{((1 - K_p)L_{pt}/2)((1 - K_s)L_{st}/2)} \end{cases} \quad (1)$$

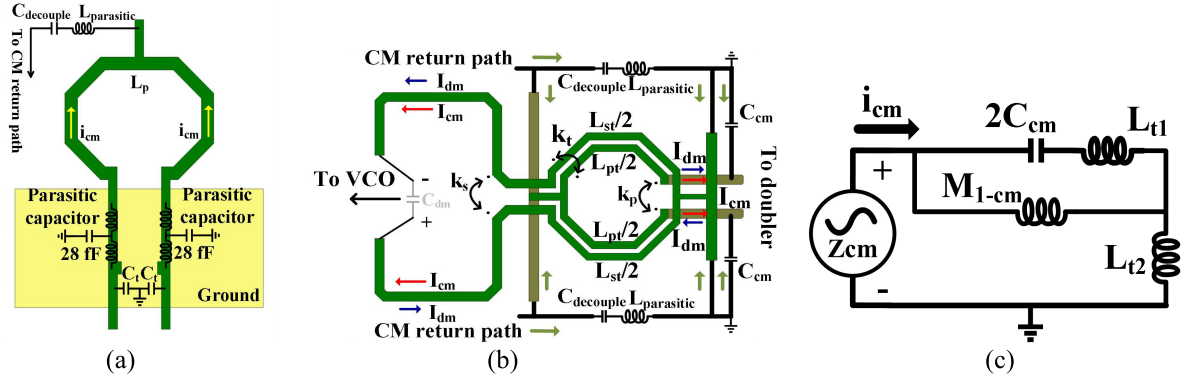


Fig. 2. (a) Layout of the implicit CM resonance. (b) Layout of the CM expansion transformer. (c) CM equivalent circuit.

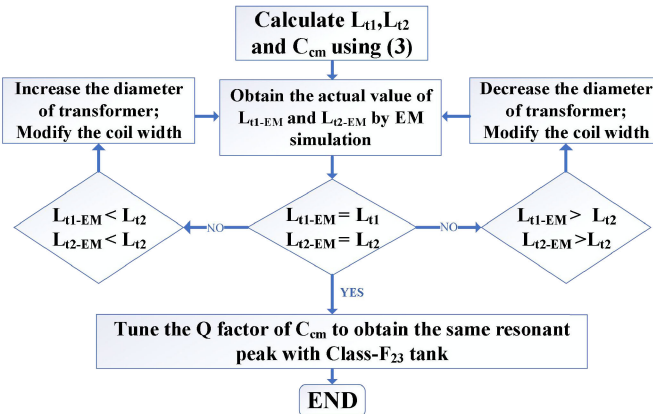


Fig. 3. Design flow of the CM expansion.

where M_{1-cm} represents the mutual inductance between L_{t1} and L_{t2} .

The following equation is the CM input impedance (Z_{cm}) according to Fig. 2(c), as (2), shown at the bottom of the page.

If we set the denominator of (2) to zero due to its second order, we can derive a resonant frequency as follows:

$$\omega_0 = \frac{1}{\sqrt{C_{cm}(L_{t1} + M_{1-cm})}}. \quad (3)$$

The design flow of the CM expansion is shown in Fig. 3. To simplify the design flow, the space between the primary and secondary coils can be set to $2 \mu m$ to obtain a fixed K_t of 0.6. Then, according to (3), one can estimate the initial value of L_{t1} , L_{t2} , and C_{cm} . The Q factor of L_{t1} and L_{t2} can be optimized by modifying the coil width. The Q factor of C_{cm} can be modified by using different metal layers.

In this design, the coil width is set to $6 \mu m$. This choice ensures that the Q factor remains similar to that of the Class-F₂₃ transformer. The CM resonant frequency of the transformer is set to about 62 GHz. According to (3), the resonant frequency can be calculated as 62 GHz when L_{t1}

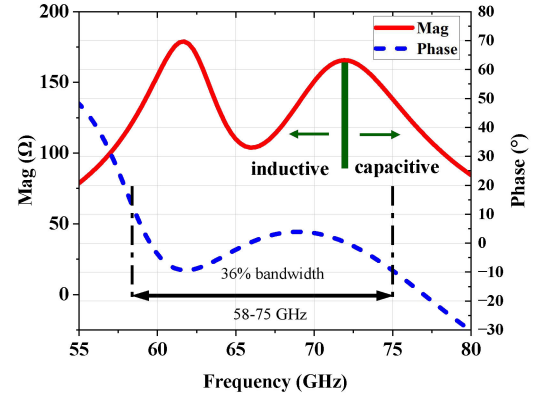


Fig. 4. Simulated Z_{11} of the CM expansion in magnitude and phase domains.

is 78 pH, M_{1-cm} is 67 pH, and C_{cm} is 45 fF. These are the initial values for the EM optimization.

Fig. 4 presents the simulated Z_{11} characteristics of the CM expansion in both the magnitude and phase domains. The first peak corresponds to the CM expansion transformer, while the second peak corresponds to the Class-F₂₃ transformer. Importantly, the Q factors of the two resonant tanks are closely matched, with a value of 5.1 for the CM expansion transformer and 4.9 for the Class-F₂₃ transformer. Then, CM Z_{11} exhibits a wideband response with a phase nearly approaching zero, spanning the frequency range of 58–75 GHz and achieving a substantial 36% bandwidth.

III. PN ANALYSIS

To validate the PN conversion mechanism using CM expansion, a Class-F₂₃ VCO without the CM expansion transformer has been designed for comparison. Three distinct frequencies, namely, 58, 71, and 75 GHz, are chosen for simulation. Among these, 58 and 75 GHz represent the lower and upper bounds of the CM expansion bandwidth, respectively, while 71 GHz is the inherent CM resonant frequency in the Class-F₂₃ tank.

$$Z_{cm} = \frac{s^3(C_{cm}L_{t1}L_{t2} + C_{cm}L_{t1}M_{1-cm} + C_{cm}L_{t2}M_{1-cm}) + s(L_{t2} + M_{1-cm})}{s^2(C_{cm}L_{t1} + C_{cm}M_{1-cm}) + 1}. \quad (2)$$

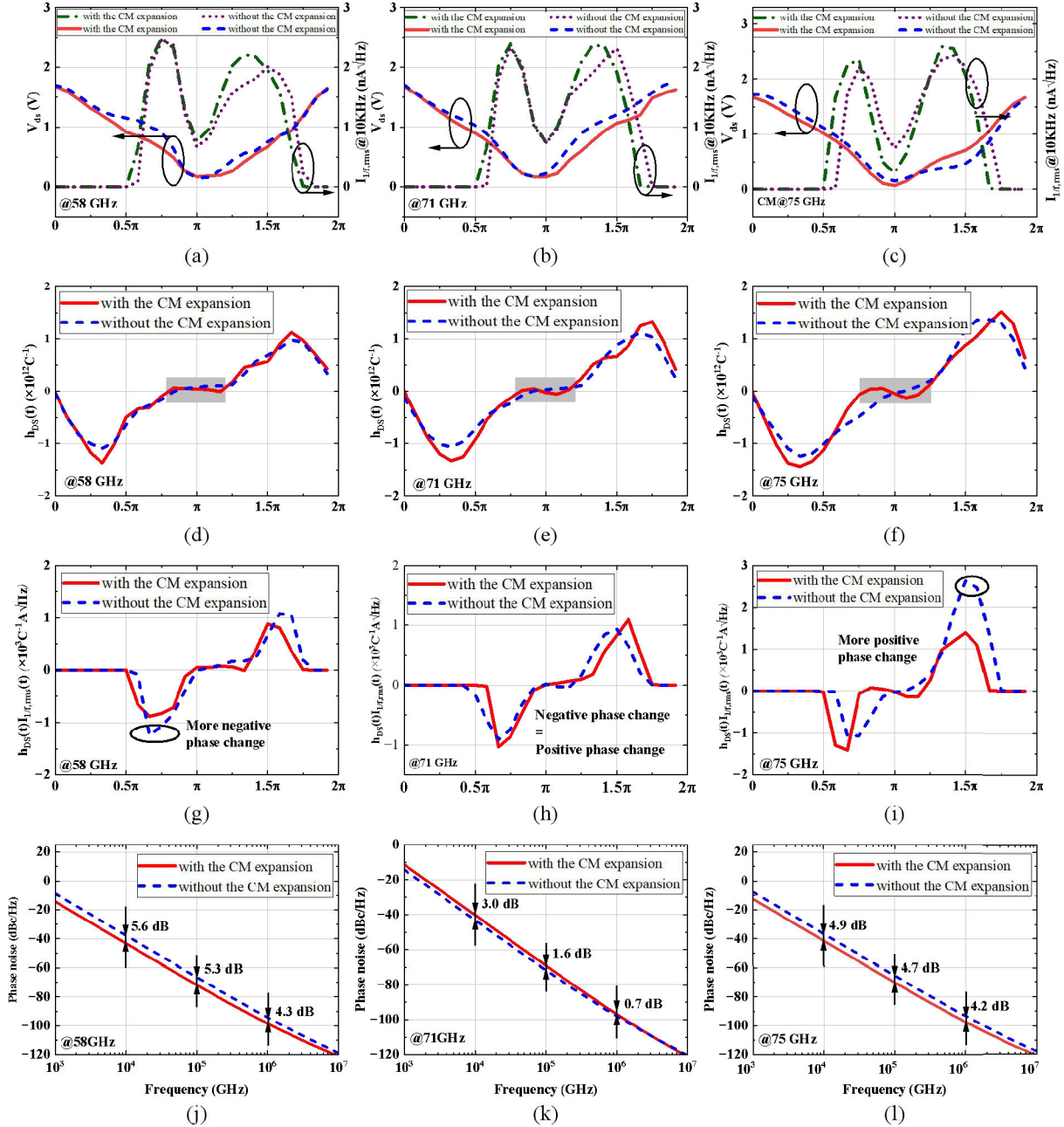


Fig. 5. Simulated (a)–(c) waveform of V_{ds} and $I_{1/f,\text{rms}}$, (d)–(f) nonnormalized ISF(h_{DS}), (g)–(i) nonnormalized effective ISF($h_{DS} \cdot I_{1/f,\text{rms}}$) within one period, and (j)–(l) PN. The simulation is conducted at 58, 71, and 75 GHz with and without the CM expansion.

A. Effects of CM Resonance Expansion for the PN

For a conventional Class-F₂₃ tank, only one CM resonant frequency existed. The CM path is inductive for the second harmonic on the left side of the CM resonant frequency (Fig. 4), the mismatch between the phase of the second harmonic and the fundamental signal results in a negative change of the nonnormalized effective impulse sensitivity function (ISF) ($h_{DS} \cdot I_{1/f,\text{rms}}$), as shown in Fig. 5(g). The falling part of V_{ds} is flattened [blue dashed line in Fig. 5(a)]. On the contrary, the CM path is capacitive for the second harmonic on the right side of the CM resonant frequency, and the mismatch results in a positive change of the nonnormalized effective ISF ($h_{DS} \cdot I_{1/f,\text{rms}}$), as shown in Fig. 5(i). The rising part of V_{ds}

TABLE I
SIMULATED AND CALCULATED PN

CM resonant frequency (GHz)		58	71	75
With CM expansion	Cal. PN@ 10 kHz (dBc/Hz)	-54.6	-52.2	-53.7
	Sim. PN@ 10 kHz (dBc/Hz)	-53.2	-50.1	-52.3
Without CM expansion	Cal. PN@ 10 kHz (dBc/Hz)	-50.4	-53.2	-50.7
	Sim. PN@ 10 kHz (dBc/Hz)	-48.7	-52.1	-47.1

is flattened in Fig. 5(c). The asymmetry of V_{ds} , which means that the positive and negative part of $h_{DS} \cdot I_{1/f,\text{rms}}$ cannot be canceled within one period, leads to a more PN upconversion.

Through our proposed CM expansion technique, the second harmonic is forced to enter the resistive path in a wideband.

TABLE II
SIMULATED AND CALCULATED NOISE CONTRIBUTIONS

Class-F ₂₃ VCO			Class-F ₂₃ VCO with CM resonance expansion			
Noise source	Value(μV ² /Hz)	Share	Noise source	Value(μV ² /Hz)	Share	
Thermal noise	N _{transistor}	3.86	10.7%	Thermal noise	2.13	6.5%
	N _{Class-F₂₃ tank}	4.36	12.2%		2.43	7.4%
N _{1/f}	24.6	68.7%	N _{1/f}	24.2	74%	
Others	3	8.4%	Others	3.6	11%	
N _{CM-expansion-tank}	/	/	N _{CM-expansion-tank}	0.37	1.1%	
N _{total}	35.82	100%	N _{total}	32.73	100%	
Phase noise conversion						
V _{carrier}	154 mV		V _{carrier}	134 mV		
PN@1 MHz (Cal.)	-95.4 dBc/Hz		PN@1 MHz (Cal.)	-94.7 dBc/Hz		
PN@1 MHz (Sim.)	-96.3 dBc/Hz		PN@1 MHz (Sim.)	-95.6 dBc/Hz		

The positive and negative changes of $h_{DS} \cdot I_{1/f,\text{rms}}$ cancel each other within one period, ensuring the symmetry of V_{ds} .

Moreover, the nonnormalized (ISF), i.e., h_{DS} , is directly proportional to the derivative of V_{ds} , and the symmetry in V_{ds} means a simultaneous symmetry in h_{DS} . The flat flat and near-zero h_{DS} in the triode region [the gray areas in Fig. 5(d)–(f)] demonstrates that the tank is insensitivity to the injected thermal noise [18], [19].

B. Numerical Verification of the PN

Fig. 5(j)–(l) indicates the simulated PN of third harmonic at 1-MHz offset. Based on the linear time-variant (LTV) PN model [20], the total noise can be classified as thermal noise of resonant tank, thermal noise of active devices, and flicker noise of transistors. The $1/f^3$ PN can be calculated according to the following equation [21]:

$$L_{1/f^3}(\Delta\omega) = \left(\frac{1}{2} \cdot \frac{\sqrt{2}}{\Delta\omega T_0} \int_0^{T_0} h_{DS}(t) \cdot I_{1/f,\text{rms}}(t) dt \right)^2 \quad (4)$$

where $h_{DS} \cdot I_{1/f,\text{rms}}$ is shown in Fig. 5(g)–(i).

Table I lists the comparison between the calculated and simulated PN corresponding to different CM resonant frequencies at 10-kHz offset. The flicker noise dominates over 90% of the PN at 10-kHz offset [22]. Then, it is reasonable to calculate the total PN using (4). In Table I, the calculated PN from (4) shows a good agreement with the simulated results. At 58 and 75 GHz, the CM expansion improves the total PN performance by suppressing the flicker noise. However, the PN of the Class-F₂₃ VCO without the CM expansion is 0.7 dB better than with the CM expansion at a 1-MHz offset in 71 GHz. This is because the CM expansion tank for Class-F₂₃ VCO is also utilized as a matching network for fundamental signal (in Section IV). The tail tank introduces extra thermal noise and leads to source degeneration of the transistors, which reduces the amplitude of the VCO voltage swing. Furthermore, Table II provides noise contributions with or without CM expansion at the frequency of 71 GHz; 1.1% noise power has been added to the Class-F₂₃ VCO by the tail tank with a 13% deterioration in the amplitude of voltage swing ($V_{carrier}$ in Table II), resulting in a 0.7-dB PN deterioration. It agrees with the results in Fig. 5(k).

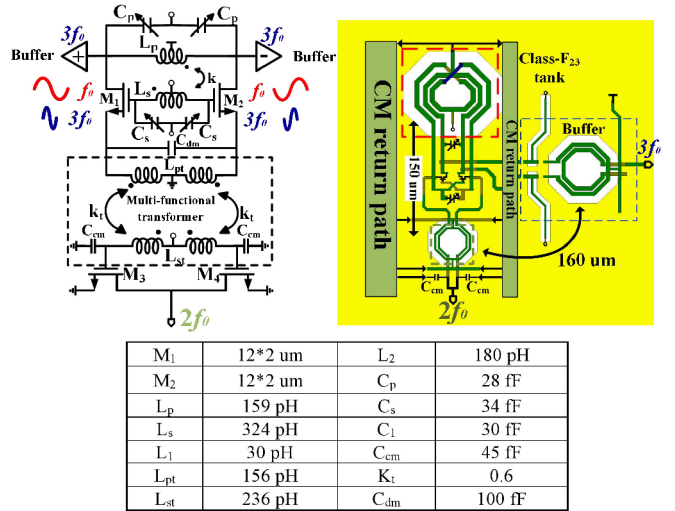


Fig. 6. Schematic and layout of the proposed dual-band VCO.

IV. CIRCUIT IMPLEMENTATION

Fig. 6 presents the schematic and layout of the proposed dual-band VCO, including a Class-F₂₃ tank, a push-push doubler, and a differential buffer amplifier. The Class-F₂₃ tank presents high impedance at both the fundamental frequency and its third harmonic. Subsequently, the third harmonic is amplified by the buffer amplifier. In parallel, the push-push doubler is responsible for generating the second harmonic. Notably, the multifunctional transformer serves a dual role, acting as a CM expansion tank and the connection between the VCO and the doubler. The distance between the multifunctional transformer and the Class-F₂₃ tank is larger than 150 μ m to avoid unwanted coupling during the layout implementation.

A. Design of 3f₀ Output

The fundamental principles of the Class-F₂₃ structure have been extensively investigated and will not be reiterated here. The conventional method for extracting the third harmonic involves ac coupling, as depicted within the blue dotted box in Fig. 7(a). However, in this context, where the third harmonics

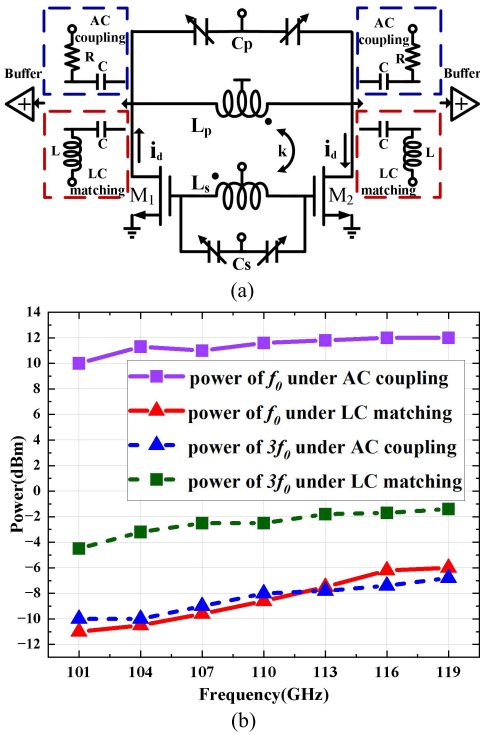


Fig. 7. (a) Schematic of ac coupling and LC matching. (b) Comparison of simulated power level at output of buffer through ac coupling and the proposed LC matching.

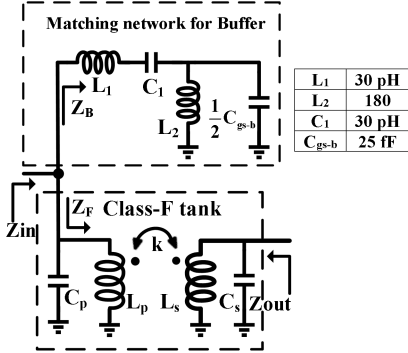


Fig. 8. Equivalent circuit of the Class-F₂₃ tank with the matching network for buffer.

reside in the W-band, the transistors exhibit lower intrinsic gain. The conventional ac coupling approach would thus compromise the output power in the W-band. To attain the desired output power, we replaced the ac coupling with an LC matching network, illustrated by the red dotted box in Fig. 7(a). In addition, the LC network can be employed as a high-pass filter to suppress the fundamental signal. Fig. 7(b) provides a comparison of the output power for both the fundamental signal and third harmonics between ac coupling and LC matching. Evidently, the power of the third harmonic is enhanced by 3 dB through the LC matching network while simultaneously achieving approximately 20 dB of suppression for the fundamental signal.

However, it is worth noting that the inclusion of the LC network at the drain nodes of the VCO transistor pair has an effect on the resonant frequencies of the Class-F₂₃ tank. Fig. 8 presents the equivalent circuit, including the Class-F₂₃ tank and the matching networks for the buffer. Here, Z_F represents

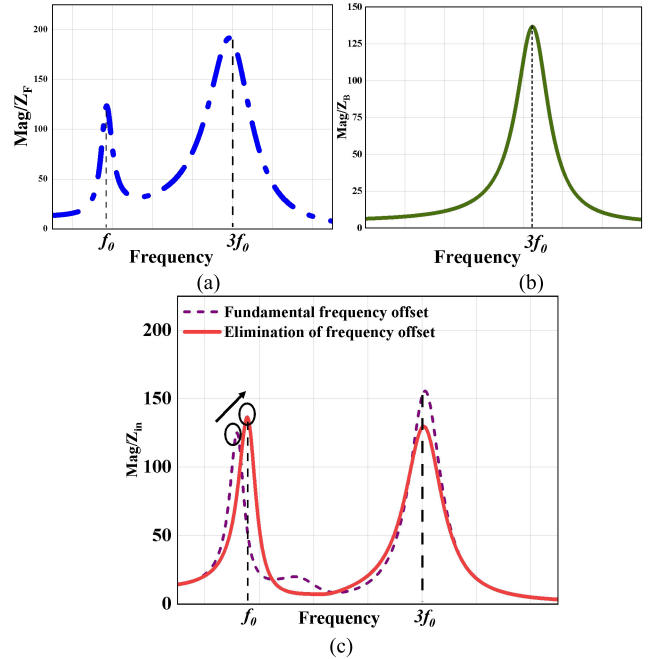


Fig. 9. Magnitude of (a) Z_F and (b) Z_B. (c) Process of eliminating the frequency offset by tuning C_s.

the input impedance of the Class-F₂₃ tank, and Z_B signifies the input impedance of the matching networks for the buffer amplifier. Considering all above, the resonant frequencies of the Class-F₂₃ tank undergo significant changes.

The input impedance Z_{in} can be calculated as follows:

$$\frac{1}{Z_{in}} = \frac{1}{Z_B} + \frac{1}{Z_F} \quad (5)$$

where Z_F is a fourth-order polynomial, i.e.,

$$Z_F = \frac{s^3 C_s L_p L_s (1 - k^2) + s L_p}{s^4 (C_p C_s L_p L_s) (1 - k^2) + s^2 (C_p L_p + C_s L_s) + 1}. \quad (6)$$

In addition, Z_B can be represented as

$$Z_B = \frac{(C_1 C_{gs-b} L_1 L_2) s^4 + (C_1 L_1 + C_1 L_2 + C_{gs-b} L_2) s^2 + 1}{(C_1 C_{gs-b} L_2) s^3 + C_1 s}. \quad (7)$$

If we set the denominator of (7) to 0, the resonant frequency of Z_B can be calculated as

$$\omega_0 = \frac{1}{\sqrt{C_{gs-b} L_2}}. \quad (8)$$

C_{gs-b} is the gate-to-source parasitic capacitor of the buffer transistor. Note that the parasitic resistances of the inductors are neglected for simplicity.

The design procedures for the Class-F₂₃ structure and matching network are elucidated as follows.

- 1) The Class-F₂₃ structure is designed in accordance with the principles outlined in reference [23], [24]. Here, the ratio of the two resonant frequencies is set at 3. The magnitude of Z_F is graphically depicted in Fig. 9(a).

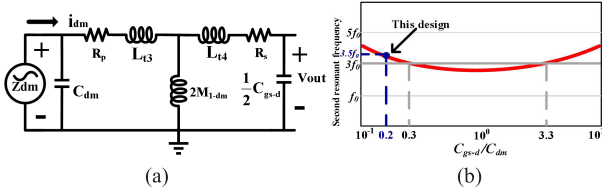


Fig. 10. (a) Equivalent circuit of the transformer in Fig. 2(b) under DM excitation. (b) Second resonant frequency versus C_{gs-d}/C_{dm} .

- 2) To attain input matching for the buffer amplifier, the resonant frequency of Z_B is configured as $3f_0$, as determined by (8). This is illustrated in Fig. 9(b).
- 3) Z_B influences the first resonant frequency of Z_{in} from (5), as indicated by the purple dashed line in Fig. 9(c). However, this frequency offset can be mitigated through the adjustment of C_s , as demonstrated by the red solid line.

By tuning C_s , the resonant frequency ratio within the Class- F_{23} tank, in conjunction with the LC matching network, is effectively maintained at 3. Consequently, the third harmonic is amplified by the buffer to generate a $3f_0$ output.

B. Design of $2f_0$ Output

A push-push doubler is implemented to generate the second harmonic at the source nodes of the VCO transistor pair, fully utilizing the strong fundamental signal.

The transformer employed for CM expansion also serves as an interconnection between the VCO and the doubler, as depicted in Fig. 6. It is crucial to determine the value of C_{dm} under DM excitation to achieve maximum transfer impedance for the fundamental frequency signal.

Fig. 10(a) illustrates the equivalent circuit for the DM of the transformer in Fig. 2(b). R_p and R_s denote the parasitic resistances of L_{pt} and L_{st} , respectively. C_{gs-d} is the gate-source capacitor of the doubler transistors. In addition, L_{t3} and L_{t4} represent the DM inductances of L_{pt} and L_{st} , respectively. These inductances can be calculated as follows:

$$\begin{cases} L_{t3} = (1 + K_p)L_{pt} - 2M_{1-dm} \\ L_{t4} = (1 + K_s)L_{st} - 2M_{1-dm} \\ M_{1-dm} = K_t \sqrt{((1 + K_p)L_{pt}/2)((1 + K_s)L_{st}/2)} \end{cases} \quad (9)$$

where M_{1-dm} is the mutual inductance between L_{t3} and L_{t4} .

The transformer conveys signals to the doubler at the differential fundamental frequency. The optimization goal is to maximize V_{out} to deliver the maximum power to the doubler. It is essential to note that i_{dm} is determined by the characteristics of the transistors and cannot be adjusted.

Therefore, V_{out} can be expressed as

$$V_{out} = i_{dm} \cdot Z_{21-dm} \quad (10)$$

where Z_{21-dm} is the transfer impedance of the transformer at the fundamental frequency.

The analysis of Z_{21-dm} can be conveniently conducted by examining the transfer impedance within the Class- F_{23} structure since they share the same structure in the DM.

The transfer impedance (Z_{21-dm}) shares resonant frequencies with the input impedance (Z_{11}) in the Class- F_{23} structure [17].

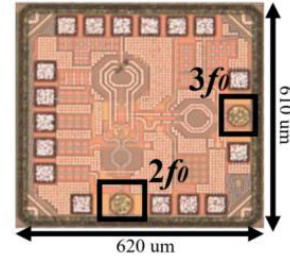


Fig. 11. Photograph of the proposed dual-band VCO.

Consequently, the analysis of Z_{21-dm} can be equivalently translated into an analysis of the resonance characteristics for Z_{11-dm} , which represents the input impedance of the transformer, as outlined next.

- 1) Z_{11-dm} exhibits two resonances, attributable to the Class- F_{23} tank. These two resonant frequencies of Z_{11-dm} can be determined as follows:

$$\omega_{1,2}^2 = \frac{1 + \left(\frac{L_{4t} C_{gs-d}}{2L_{3t} C_{dm}} \right) \pm \sqrt{1 + \left(\frac{L_{4t} C_{gs-d}}{2L_{3t} C_{dm}} \right)^2 + \left(\frac{L_{4t} C_{gs-d}}{2L_{3t} C_{dm}} \right) (4k_t^2 - 2)}}{L_{4t} C_{gs-d} (1 - k_t^2)}. \quad (11)$$

- 2) The first resonant frequency of Z_{11-dm} can be set by tuning C_{dm} , which, in this design, is configured at 100 fF. This adjustment ensures the maximum transfer impedance at the fundamental frequency.
- 3) To ensure that the second resonant frequency is sufficiently distant from $3f_0$, thus preventing third harmonic leakage. Notably, as the first resonant frequency corresponds to the fundamental frequency and L_{3t} and L_{4t} are roughly equalized, the second resonant frequency is influenced by C_{gs-d}/C_{dm} according to (11).

Fig. 10(b) presents the relationship between the second resonant frequency and C_{gs-d}/C_{dm} . In this specific design, C_{gs-d} is determined by the doubler transistors and is set at 20 fF, while C_{dm} measures 100 fF, as determined from the earlier. Therefore, C_{gs-d}/C_{dm} is equal to 0.2. The second resonant frequency is $3.5f_0$ from Fig. 10(b).

V. MEASUREMENT RESULTS

The proposed dual-band VCO has been manufactured using 40-nm CMOS technology. As depicted in Fig. 11, the VCO is shown in a photograph where the $3f_0$ output is positioned on the right side, and the $2f_0$ output is located at the bottom. The overall chip dimensions, including the dc/ground pads and decoupling capacitors, measure $620 \times 610 \mu\text{m}$. In terms of power consumption, the VCO consumes 44 mW under a 0.9-V supply voltage, which includes the buffer stage. On-wafer measurements were conducted using a GSG probe and a 1-mm 110-GHz cable to connect the VCO's output GSG port to an R&S FSW spectrum analyzer.

For frequency tuning, the varactors are biased within the range of -0.9 to 0.9 V, with a step increment of 0.1 V. Fig. 12(a) illustrates a tuning range of 5.7%, spanning from 104.88 to 110.75 GHz at the $3f_0$ output node.

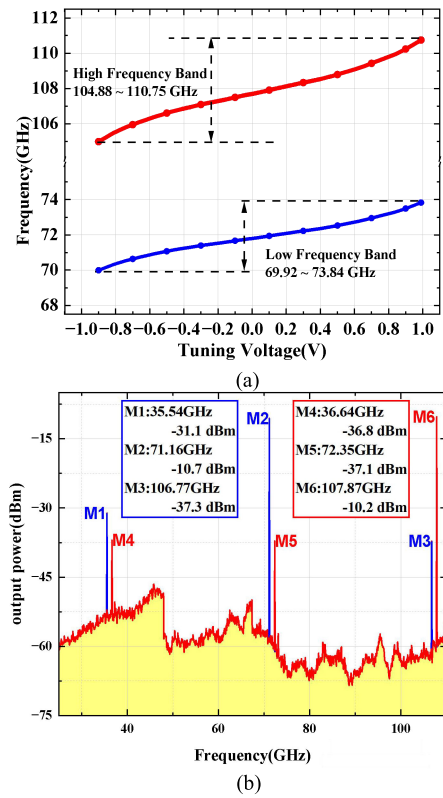


Fig. 12. (a) Frequency tuning range of the dual-band VCO. (b) Spectrum at the $2f_0$ and $3f_0$ output nodes.

Similarly, a tuning range of 5.7%, extending from 69.92 to 73.84 GHz, is achieved at the $2f_0$ output node. The curves are obtained by tuning different values of C_s and C_p . Further enhancement of the tuning range can be realized through the utilization of a switched capacitor array.

The spectrum, measured with power calibration at both the $2f_0$ and $3f_0$ outputs, is illustrated in Fig. 12(b). To clearly distinguish between them, the $2f_0$ and $3f_0$ output spectra are obtained under different tuning voltages, resulting in a slight frequency offset. M_1 – M_3 (blue line) represent the spectrum at the $2f_0$ output, while M_4 – M_6 (red line) correspond to the spectrum at the $3f_0$ output. The output powers at both $2f_0$ and $3f_0$ are -10 dBm. With the application of our LC matching network and one-stage differential buffer, the subharmonics measure approximately 20–25 dBc. To achieve even better subharmonic suppression, additional stages of amplification can be employed [24].

Fig. 13(a) exhibits the measured PN of the proposed dual-band VCO, while Fig. 13(b) presents the PN of the Class- F_{23} VCO without CM expansion for comparison. At the 105-GHz output, the PN of the proposed dual-band VCO is -92 dBc/Hz at a 1-MHz offset, representing a 4-dB improvement over the Class- F_{23} VCO without CM expansion. Furthermore, at the 70-GHz output, the proposed dual-band VCO attains a PN of -102 dBc/Hz at a 1-MHz offset. The CM expansion technique yields a $1/f^3$ flicker noise corner of 244 kHz for the proposed dual-band VCO, outperforming the Class- F_{23} VCO without CM expansion (571 kHz). Fig. 14 displays the measured PN, power, FoM, and fundamental signal suppression versus frequency for both VCOs.

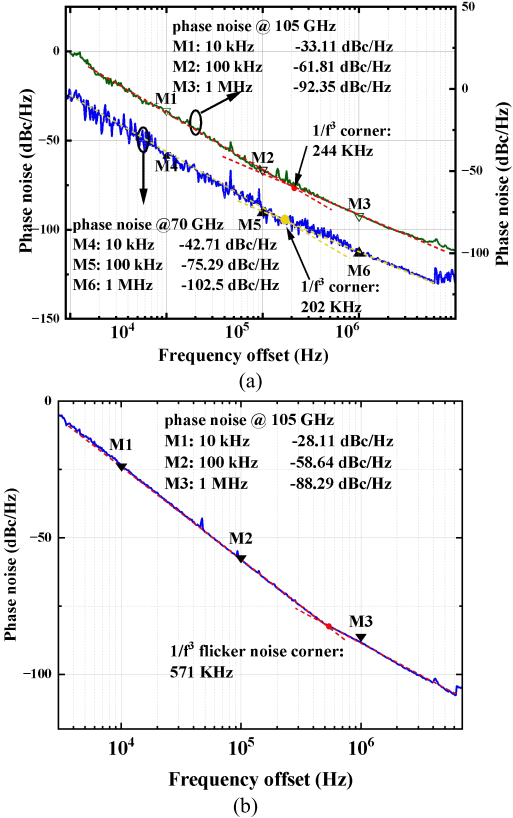


Fig. 13. Measured PN of (a) proposed VCO at 70 and 105 GHz and (b) conventional Class- F_{23} VCO for comparison.

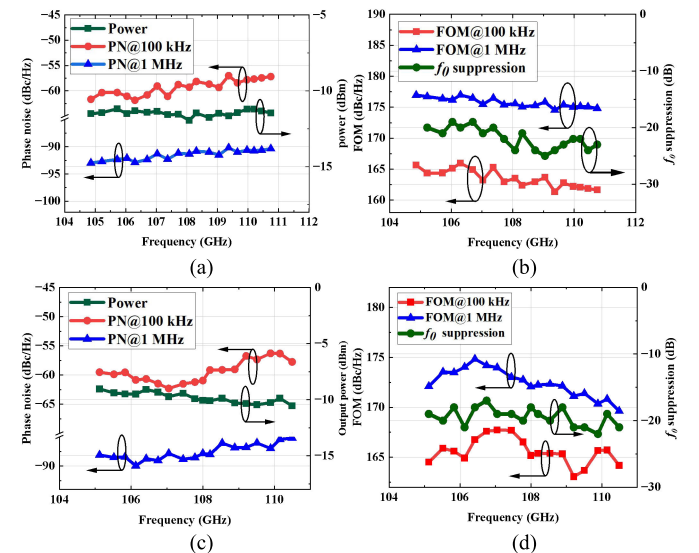


Fig. 14. Measured PN, output power, FoM, and f_0 suppression versus frequency of (a) and (b) proposed dual-band VCO at $3f_0$ output and (c) and (d) Class- F_{23} VCO without CM expansion for comparison.

In Fig. 14(a) and (b), the introduction of CM expansion leads to reduced variations in both PN and FoM at $3f_0$ output. In Fig. 14(c) and (d), which pertain to Class- F_{23} VCO without CM expansion, the PN experiences a rapid deterioration at frequencies out of the CM resonance. In addition, Fig. 15 shows the VCO performance at $2f_0$ output. As the dual band is generated from one transformer, the performance at $2f_0$

TABLE III
COMPARISONS OF THE DUAL-BAND VCO WITH STATE-OF-THE-ART

Ref.	Process	Frequency (GHz)	Tuning Range (%)	P _{DC} (mW)	Area (mm ²)	Phase Noise @ 1MHz (dBc/Hz)	⁽¹⁾ FoM (dBc/Hz)	⁽²⁾ FoM _T (dBc/Hz)	1/f ³ corner (kHz)
V band VCOs									
[2]	65nm CMOS	62	26.2	7.4 to 11.2	0.0395	⁽³⁾ -87.2 to -96.3	-172.6 to -183.5	-180.9 to -183.5	⁽⁶⁾ 991
[25]	65nm CMOS	70.2	22.3	7.7 to 8.8	0.013	-85.8 to -92	-173.3 to -180.4	-180.3 to -187.4	/
[26]	65nm CMOS	55	18	6.2	0.06	-89.9	⁽⁴⁾ -178.9	⁽⁴⁾ -184	/
[27]	65nm CMOS	73	22.8	10.2	0.03	⁽³⁾ -86.7 to -94.6	-173.9 to -181.9	-181 to -189	1000
[28]	65nm CMOS	59.8	14.5	9	0.12	-100.7	-186.7	-175.2	580
[24]	40nm CMOS	55	25.4	45	0.13	-100.1	-181.5	-189.6	950
This Work	40nm CMOS	70	5.7	44	⁽⁵⁾ 0.36	-102	-182.5	-178	202
W band VCOs									
[29]	65 nm CMOS	105	20.7	65.5	0.42	-98	-180.2	-186.6	630
[30]	65nm CMOS	89.3	8.3	8.5	0.25	-91.8	-181.5	-179.8	/
[31]	65 nm CMOS	102	3	8	0.16	-86.3	-177.4	-167.0	/
[32]	65 nm CMOS	103	11.4	22.5	0.39	-88	⁽⁴⁾ -183.4 to -163	-174 to -157.4	/
[33]	28 nm CMOS	102	14.1	62.21	0.035	-83.1	⁽⁴⁾ -171.4 to -163.3	-174.4 to -166.3	/
This Work	40 nm CMOS	105	5.7	44	⁽⁵⁾ 0.36	-92	-176	-171.5	244

$$^{(1)}FoM = -L(\Delta f) + 10 \log\left(\frac{f_0^2}{\Delta f^2} \cdot \frac{1mW}{P_{DC}}\right), ^{(2)}FoM_T = FoM + 20 \log\left(\frac{TR}{10}\right), \text{ where } L(\Delta f) \text{ is the PN at the offset frequency } \Delta f, f_0 \text{ is the operating frequency, } \\ \Delta f \text{ is the power consumption and TR is the frequency tuning range. } ^{(3)}\text{The PN is estimated from 10 MHz offset. } ^{(4)}\text{The FoM is measured at 10 MHz offset. } \\ ^{(5)}\text{The area including buffer and doubler together with large decoupling capacitors and DC pads. } ^{(6)}\text{The } 1/f^3 \text{ corner is estimated from measured curve.}$$

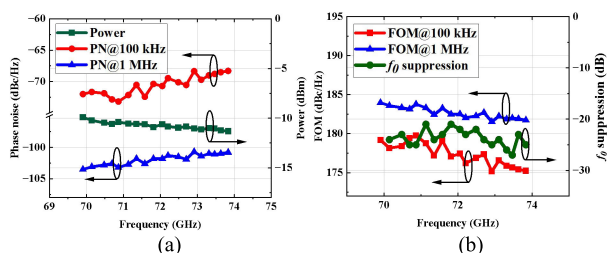


Fig. 15. Measured (a) PN and output power and (b) FoM and f_0 suppression versus frequency of the proposed dual-band VCO at $2f_0$ output.

and $3f_0$ shows a good correspondence. Fig. 16 shows the measured $1/f^3$ PN corner of Class F₂₃ VCO with/without the CM expansion. It can be found that the CM expansion has a better $1/f^3$ corner.

Table III provides a performance comparison of the dual-band VCO with state-of-the-art designs. The dual bands are compared individually as there are no other designs with similar frequency bands for direct comparison. Our proposed VCO excels in PN performance at both frequencies, thanks to the utilization of CM resonance expansion. As our work adopts a conservative varactor design, the tuning range is

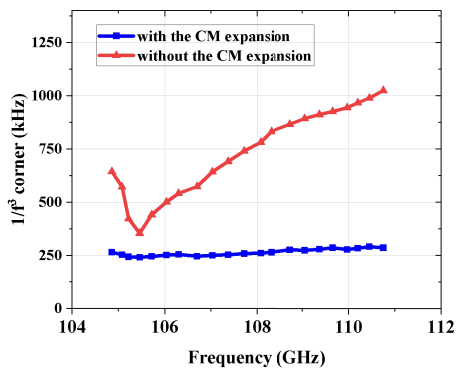


Fig. 16. Measured $1/f^3$ PN corner of Class F₂₃ VCO with/without the CM expansion.

limited. However, more varactors or switch capacitor arrays can be added to the proposed VCO to expand the bandwidth without significantly impacting the PN performance. While some designs achieve superior PN and tuning range through the application of multiresonance, multicore, and multimode techniques [29], they often come at the cost of higher power consumption or chip area.

VI. CONCLUSION

In this article, we present the design of a low-phase-noise dual-band VCO operating in the V - and W -bands. A frequency ratio of 1.5 is achieved through the incorporation of a Class-F₂₃ tank, a push-push doubler, and switchless. The key innovation lies in the use of a multifunctional transformer, which offers high transfer impedance for the signal at the fundamental frequency and facilitates CM resonance expansion for PN reduction. This expanded CM resonance effectively suppresses the flicker noise upconversion across a broad bandwidth, eliminating the need for manual harmonic tuning.

A comparative analysis with the Class-F₂₃ VCO without CM expansion has also been conducted, highlighting the advantages of our proposed design. The VCO demonstrates impressive frequency coverage, spanning from 69.92 to 73.84 GHz and from 104.88 to 110.75 GHz, with tuning ranges of 5.7%. Furthermore, the measured PNs are measured at -102.5 and -92.35 dBc/Hz at a 1-MHz offset, accompanied by FoMs of -182.5 and -176 dBc/Hz, respectively. Despite its performance capabilities, the VCO maintains a power consumption of 44 mW and occupies an area of 0.36 mm^2 .

REFERENCES

- [1] S. Wang and G. M. Rebeiz, "Dual-band 28- and 39-GHz phased arrays for multistandard 5G applications," *IEEE Trans. Microw. Theory Techn.*, vol. 71, no. 1, pp. 339–349, Jan. 2023.
- [2] A. Basaligheh, P. Saffari, W. Winkler, and K. Moez, "A wide tuning range, low phase noise, and area efficient dual-band millimeter-wave CMOS VCO based on switching cores," *IEEE Trans. Circuits Syst. I, Reg. Papers*, vol. 66, no. 8, pp. 2888–2897, Aug. 2019.
- [3] S. Oh, K.-S. Seo, and J. Oh, "Low phase noise concurrent dual-band (5/7 GHz) CMOS VCO using gate feedback on nonuniformly wound transformer," *IEEE Microw. Wireless Compon. Lett.*, vol. 31, no. 2, pp. 177–180, Feb. 2021.
- [4] J. Baylon, P. Agarwal, L. Renaud, S. N. Ali, and D. Heo, "A Ka-band dual-band digitally controlled oscillator with -195.1 -dBc/Hz FoMT based on a compact high- Q dual-path phase-switched inductor," *IEEE Trans. Microw. Theory Techn.*, vol. 67, no. 7, pp. 2748–2758, Jul. 2019.
- [5] S.-L. Jang and S. Jain, "Dual C- and S-band CMOS VCO using the shunt varactor switch," *IEEE Trans. Very Large Scale Integr. (VLSI) Syst.*, vol. 23, no. 9, pp. 1808–1813, Sep. 2015.
- [6] I. Mansour et al., "Dual-band VCO using high quality factor two orthogonally located inductors in $0.18\text{-}\mu\text{m}$ CMOS technology," *IEEE Microw. Wireless Compon. Lett.*, vol. 32, no. 12, pp. 1431–1434, Dec. 2022.
- [7] S. Jain, S.-L. Jang, and N. T. Tchamov, "Tuned LC-resonator dual-band VCO," *IEEE Microw. Wireless Compon. Lett.*, vol. 26, no. 3, pp. 204–206, Mar. 2016.
- [8] M. Vigilante and P. Reynaert, "A dual-band E-band quadrature VCO with switched coupled transformers in 28 nm HPM bulk CMOS," in *Proc. IEEE Radio Freq. Integr. Circuits Symp. (RFIC)*, Phoenix, AZ, USA, May 2015, pp. 119–122.
- [9] B. Li, Y. Liu, C. Yu, and Y. Wu, "Independent control function for concurrent dual-band VCO," *IEEE Microw. Wireless Compon. Lett.*, vol. 28, no. 3, pp. 230–232, Mar. 2018.
- [10] R. Zhang, Z. Chen, Z. Li, D. Hou, J. Chen, and W. Hong, "A wide tuning range low-phase-noise Ku/Ka dual bands SiGe VCO based on transformer-coupled tank," *IEEE Microw. Wireless Compon. Lett.*, vol. 32, no. 5, pp. 437–440, May 2022.
- [11] Y. Chen, P.-I. Mak, and R. P. Martins, "High-performance harmonic-rich single-core VCO with multi-LC tank: A tutorial," *IEEE Trans. Circuits Syst. II, Exp. Briefs*, vol. 69, no. 7, pp. 3115–3121, Jul. 2022.
- [12] Y. Hu, T. Siriburanon, and R. B. Staszewski, "A low-flicker-noise 30-GHz class-F₂₃ oscillator in 28-nm CMOS using implicit resonance and explicit common-mode return path," *IEEE J. Solid-State Circuits*, vol. 53, no. 7, pp. 1977–1987, Jul. 2018.
- [13] J. Du et al., "A compact 0.2–0.3-V inverse-class-F₂₃ oscillator for low 1/f₃ noise over wide tuning range," *IEEE J. Solid-State Circuits*, vol. 57, no. 2, pp. 452–464, Feb. 2022.
- [14] D. Murphy, H. Darabi, and H. Wu, "Implicit common-mode resonance in LC oscillators," *IEEE J. Solid-State Circuits*, vol. 52, no. 3, pp. 812–821, Mar. 2017.
- [15] Z. Zong, G. Mangraviti, and P. Wambacq, "Low 1/f₃ noise corner LC-VCO design using flicker noise filtering technique in 22 nm FD-SOI," *IEEE Trans. Circuits Syst. I, Reg. Papers*, vol. 67, no. 5, pp. 1469–1480, May 2020.
- [16] M. Shahmohammadi, M. Babaie, and R. B. Staszewski, "A 1/f noise upconversion reduction technique for voltage-biased RF CMOS oscillators," *IEEE J. Solid-State Circuits*, vol. 51, no. 11, pp. 2610–2624, Nov. 2016.
- [17] Z. Lin, H. Jia, R. Ma, W. Deng, Z. Wang, and B. Chi, "A low-phase-noise VCO with common-mode resonance expansion and intrinsic differential 2nd-harmonic output based on a single three-coil transformer," *IEEE J. Solid-State Circuits*, vol. 59, no. 1, pp. 253–267, Jan. 2023, doi: [10.1109/JSSC.2023.3274178](https://doi.org/10.1109/JSSC.2023.3274178).
- [18] F. Hong, H. Zhang, and D. Zhao, "An X-band CMOS VCO using ultra-wideband dual common-mode resonance technique," *IEEE Trans. Circuits Syst. I, Reg. Papers*, vol. 69, no. 9, pp. 3579–3590, Sep. 2022.
- [19] H. Guo, Y. Chen, P.-I. Mak, and R. P. Martins, "20.1 A 5.0-to-6.36 GHz wideband-harmonic-shaping VCO achieving 196.9dBc/Hz peak FoM and 90-to-180 kHz 1/f₃ PN corner without harmonic tuning," in *Proc. IEEE Int. Solid-State Circuits Conf. (ISSCC)*, vol. 64, San Francisco, CA, USA, Feb. 2021, pp. 294–296.
- [20] A. Hajimiri and T. H. Lee, "A general theory of phase noise in electrical oscillators," *IEEE J. Solid-State Circuits*, vol. 33, no. 2, pp. 179–194, Feb. 1998.
- [21] Y. Hu, T. Siriburanon, and R. B. Staszewski, "Oscillator flicker phase noise: A tutorial," *IEEE Trans. Circuits Syst. II, Exp. Briefs*, vol. 68, no. 2, pp. 538–544, Feb. 2021.
- [22] J. Gong, Y. Chen, E. Charbon, F. Sebastian, and M. Babaie, "A cryo-CMOS oscillator with an automatic common-mode resonance calibration for quantum computing applications," *IEEE Trans. Circuits Syst. I, Reg. Papers*, vol. 69, no. 12, pp. 4810–4822, Dec. 2022.
- [23] M. Babaie and R. B. Staszewski, "A class-F CMOS oscillator," *IEEE J. Solid-State Circuits*, vol. 48, no. 12, pp. 3120–3133, Dec. 2013.
- [24] Z. Zong, M. Babaie, and R. B. Staszewski, "A 60 GHz frequency generator based on a 20 GHz oscillator and an implicit multiplier," *IEEE J. Solid-State Circuits*, vol. 51, no. 5, pp. 1261–1273, May 2016.
- [25] Y. Chao and H. C. Luong, "Analysis and design of wide-band millimeter-wave transformer-based VCO and ILFDs," *IEEE Trans. Circuits Syst. I, Reg. Papers*, vol. 63, no. 9, pp. 1416–1425, Sep. 2016.
- [26] M. H. Kashani, A. Tarkeshdouz, R. Molavi, A. Sheikholeslami, E. Afshari, and S. Mirabbasi, "On the design of a high-performance mm-wave VCO with switchable triple-coupled transformer," *IEEE Trans. Microw. Theory Techn.*, vol. 67, no. 11, pp. 4450–4464, Nov. 2019.
- [27] A. Basaligheh, P. Saffari, I. M. Filanovsky, and K. Moez, "A 65–81 GHz CMOS dual-mode VCO using high quality factor transformer-based inductors," *IEEE Trans. Circuits Syst. I, Reg. Papers*, vol. 67, no. 12, pp. 4533–4543, Dec. 2020.
- [28] C. Fan, J. Yin, C. -C. Lim, P. -I. Mak, and R. P. Martins, "17.9 A 9mW 54.9-to-63.5 GHz current-reuse LO generator with a 186.7dBc/Hz FoM by unifying a 20 GHz 3rd-harmonic-rich current-output VCO, a harmonic-current filter and a 60 GHz TIA," in *IEEE Int. Solid-State Circuits Conf. (ISSCC)*, San Francisco, CA, USA, 2020, pp. 282–284.
- [29] H. Guo, Y. Chen, Y. Huang, P.-I. Mak, and R. P. Martins, "8.4 an 83.3-to-104.7GHz harmonic-extraction VCO incorporating multi-resonance, multi-core, and multi-mode (3M) techniques achieving -124dBc/Hz absolute PN and 190.7dBc/Hz FoMT," in *IEEE Int. Solid-State Circuits Conf. (ISSCC) Dig. Tech. Papers*, San Francisco, CA, USA, Feb. 2023, pp. 152–154.
- [30] A. Tarkeshdouz, M. H. Kashani, E. Hadizadeh Hafshejani, S. Mirabbasi, and E. Afshari, "An 82.2-to-89.3 GHz CMOS VCO with DC-to-RF efficiency of 14.8%," in *Proc. IEEE Radio Freq. Integr. Circuits Symp. (RFIC)*, Boston, MA, USA, Jun. 2019, pp. 331–334.
- [31] S. Yoo et al., "23.4 an 82fsrms-jitter and 22.5 mW-power, 102GHz W-band PLL using a power-gating injection-locked frequency-multiplier-based phase detector in 65 nm CMOS," in *IEEE Int. Solid-State Circuits Conf. (ISSCC) Dig. Tech. Papers*, San Francisco, CA, USA, Feb. 2021, pp. 330–331.

- [32] Y. Chao, H. C. Luong, and Z. Hong, "Analysis and design of a 14.1-mW 50/100-GHz transformer-based PLL with embedded phase shifter in 65-nm CMOS," *IEEE Trans. Microw. Theory Techn.*, vol. 63, no. 4, pp. 1193–1201, Apr. 2015.
- [33] S. Oh, J. Kim, and J. Oh, "W-band switch-less reconfigurable-push dual-band VCO using clover-shaped inductor and robust triple cores for 6G communications," *IEEE Trans. Microw. Theory Techn.*, vol. 71, no. 5, pp. 1890–1898, May 2023.



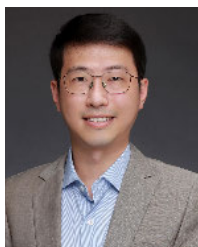
Dongxin Ni (Graduate Student Member, IEEE) received the B.S. degree in electronic science and technology from Southeast University (SEU), Nanjing, China, in 2017, and the M.S. degree from the China Electronics Technology Group Corporation No.58 Institute, Nanjing, in 2020. He is currently pursuing the Ph.D. degree in electronic science and technology at Shanghai Jiao Tong University (SJTU), Shanghai, China.

His current research interests include millimeter-wave transceivers and low-phase-noise multibands voltage-controlled oscillators (VCOs). In addition, he focuses on 3-D heterogeneous integration packaging for millimeter-wave transceivers and proposes theoretical modeling and design methods of 3-D packaged integrated circuit.



Zhe Zhao (Graduate Student Member, IEEE) received the B.S. degree in electronic information engineering from Harbin Engineering University (HEU), Harbin, China, in 2016, and the M.S. degree in electrical engineering from The University of Melbourne (UoFTEL), Melbourne, VIC, Australia, in 2019. He is currently pursuing the Ph.D. degree in electronic science and technology at Shanghai Jiao Tong University, Shanghai, China.

His current research interests include millimeter-wave and sub-terahertz ICs design for 3-D system-on-package applications.



Liang Zhou (Senior Member, IEEE) received the Ph.D. degree in electrical engineering from the University of York, York, U.K., in 2005.

At the University of York, he was working on ultralow-phase-noise oscillators. From 2005 to 2006, he was a Senior RF Engineer with Motorola INC, Shanghai, China, where he was involved in power amplifier design for the next generation of base station transceivers. He was a Visiting Scholar with the Massachusetts Institute of Technology, Cambridge, MA, USA, in 2007. From February 2017, he was a Research Fellow with the Institute for Electronics Engineering (LTE), Friedrich-Alexander-University Erlangen-Nürnberg, Erlangen, Germany, granted by the Alexander von Humboldt-Stiftung. He is a Full Professor of the Key Laboratory of Ministry of Education of Design and Electromagnetic Compatibility of High-Speed Electronic Systems, Shanghai Jiao Tong University, Shanghai. His main research interests include system on packaging (SOP) design and modeling, EMC and high-power microwave (HPM) protection of communication platforms, and multi-physics and its application.

Dr. Zhou was the recipient of National Science Fund for Excellent Young Scholars in 2018, Alexander von Humboldt (AvH) research fellowship in 2016, APEMC Young Scientist Award in 2016, the Research Grant of the Okawa Foundation (Japan) in 2016, the International Union of Radio Science (URSI), Young Scientist Award in 2014, the best paper awards of Cross Strait Quad-Regional Radio Wireless Conference (CSQRWC) in 2014, and the National Science and Technology Advancement Award of China in 2012. He was the IEEE EMC Distinguished Lecturer from 2019 to 2020 and the IEEE EMC Shanghai Chapter Chair.



Jian Pang (Member, IEEE) received the bachelor's and master's degrees from Southeast University, Nanjing, China, in 2012 and 2014, respectively, and the Ph.D. degree from the Department of Physical Electronics, Tokyo Institute of Technology, Tokyo, Japan, in 2019.

From 2019 to 2020, he was a Post-Doctoral Researcher with the Tokyo Institute of Technology. From 2020 to 2022, he was a Special-Appointed Assistant Professor with the Tokyo Institute of Technology. From 2022 to 2023, he was a Special-Appointed Associate Professor with the Tokyo Institute of Technology. He is currently an Associate Professor with Shanghai Jiao Tong University, Shanghai, China, focusing on 5G millimeter-wave systems. His current research interests include high-data-rate low-cost millimeter-wave transceivers, power-efficient power amplifiers for 5G mobile systems, multiple-in–multiple-out (MIMO), and mixed-signal calibration systems.

Dr. Pang was a recipient of the IEEE Solid-State Circuits Society Student Travel Grant Award in 2016, the IEEE SSCS Pre-Doctoral Achievement Award for the term 2018–2019, the Seiichi Tejima Oversea Student Research Award in 2020, and the IEEE Microwave Theory and Techniques Society Japan Young Engineer Award in 2021.



Jun-Fa Mao (Fellow, IEEE) was born in 1965. He received the B.S. degree in radiation physics from the National University of Defense Technology, Changsha, China, in 1985, the M.S. degree in experimental nuclear physics from the Shanghai Institute of Nuclear Research, Chinese Academy of Sciences, Shanghai, China, in 1988, and the Ph.D. degree in electronic engineering from Shanghai Jiao Tong University, Shanghai, in 1992.

From July 1992 to January 2022, he was a Faculty Member with Shanghai Jiao Tong University, where he was a Chair Professor. He was the Dean and the Vice President of the School of Electronic Information and Electrical Engineering, Shanghai Jiao Tong University. He was a Visiting Scholar with the Chinese University of Hong Kong, Hong Kong, from 1994 to 1995, and a Post-Doctoral Researcher with the University of California at Berkeley, Berkeley, CA, USA, from 1995 to 1996. Since 2022, he has been the President of Shenzhen University, Shenzhen, China. He has authored or coauthored more than 600 articles (including more than 160 IEEE journal articles). His research interests include the interconnect and package problem of integrated circuits and systems and analysis and design of microwave components and circuits.

Dr. Mao was a member of the 2012–2014 IEEE Microwave Theory and Techniques Society Fellow Evaluation Committee and the 2015 IEEE Fellow Committee. He is a member of the State Council Academic Degrees Committee. He is a Fellow of CIE. He is an academician of the Chinese Academy of Science. He was a recipient of the National Natural Science Award of China in 2004, the National Technology Invention Award of China in 2008, the National Science and Technology Advancement Award of China in 2012, the Top Ten Scientific and Technological Progress of Chinese Universities in 2020, and six best paper awards of international conferences. He was also a recipient of the two National Awards of Teaching in 2005 and 2018. He is a Chief Scientist of the National Basic Research Program (973 Program) of China; a Project Leader of the Natural Science Foundation of China for Creative Research Groups; a Cheung Kong Scholar of the Ministry of Education, China; the Director of the Microwave Society of China Institute of Electronics; and the 2009–2018 Chair of IEEE MTT-S Shanghai Chapter. He was the Founder and the 2007–2009 Chair of the IEEE Shanghai Section.